JOURNAL OF THERMOPHYSICS AND HEAT TRANSFER
Vol. 17, No. 2, April–June 2003

Microscale Transport Processes in the Evaporator of a Constrained Vapor Bubble

Ling Zheng,* Ying-Xin Wang,† Peter C. Wayner Jr.,‡ and Joel L. Plawsky§
Rensselaer Polytechnic Institute, Troy, New York 12180-3590

Microgravity experiments on a constrained vapor bubble heat exchanger (CVB) are being developed for the space station. Results are presented of precursory experiments and modeling on microscale transport processes in the evaporator of the vertical constrained vapor bubble in the Earth's environment. A nonisothermal experimental setup was designed and built to study heat transfer and fluid flow in an ethanol/quartz vertical CVB system. Temperature profiles were measured using an in situ LabView® data acquisition system via thermocouples. Film thickness profiles were measured using image analyzing interferometry. A mathematical model was developed to yield the liquid film curvature profile in the evaporator. Experimentally measured curvature profiles were in good agreement with modeling results. A theoretical relation between the curvature and temperature profiles in the Earth's environment was developed. Under microgravity conditions, an analytical expression that reveals an inherent relation between temperature and liquid film curvature profiles was derived for the first time.

Nomenclature

A = area, m^2
B = dispersion constant, J · m
C_l = geometric coefficient
c = contact line length, m
d_h = hydraulic diameter of the flow channel, m
f = friction factor
g = acceleration due to gravity, m/s^2
h_{fg} = latent heat of vaporization, J/kg
h_o = heat transfer coefficient between constrained vapor bubble heat exchanger (CVB) and room, W/m^2s
K = curvature of liquid film, m^{-1}
k = thermal conductivity, W/mK
k_f = friction factor coefficient
L_{lw} = length of liquid–wall interface, m
m = rate of evaporation, kg/m · s
N = number of fringes
P = pressure, Pa
p = perimeter, m
Q = power of heater to the CVB, W
r = radius of curvature, m
T = temperature, °C
U = velocity, m/s
V = vapor in the CVB
x = axial distance, m
y = distance in the direction normal to CVB axis, m
z = distance in the direction normal to CVB axis, perpendicular to y axis, m
α = angle at the corner of the CVB cell
β = inclination angle
Γ = total rate of evaporation, kg/s
ΔP = pressure difference, Pa
δ = liquid film thickness, m
θ = apparent contact angle
μ = viscosity, Pa · s
Π = disjoining pressure, Pa
ρ = density, kg/m^3
σ = surface tension, N/m
τ = shear stress, Pa
ϕ = angle covered by the arc of the meniscus at the corner of the CVB cell

Subscripts

c = corner of the CVB cell
cal = calculated results
exp = experimental results
i = number of fringes
l = liquid
lw = liquid–wall
o = outside cell
v = vapor
vw = vapor–wall
1 = arbitrary location 1 along the length of the CVB
2 = arbitrary location 2 along the length of the CVB
∞ = environment

Introduction

THE use of interfacial free energy gradients to control fluid flow naturally leads to simpler and lighter heat transfer systems because of the absence of mechanical pumps. Therefore, "passive" engineering systems based on this principle are ideal candidates for a microgravity environment. In this context, passive refers to the natural pressure field for fluid flow due to changes in the intermolecular force field resulting from an imposed nonisothermal temperature field. This force field is a function of the shape, temperature, and composition of the system. Passive systems that depend on regions with low capillary pressures are emphasized herein. In particular, we are concerned with experimental and theoretical studies of a passive constrained vapor bubble heat exchanger (CVB) system presented in Fig. 1. The liquid–vapor system is formed by evacuating a closed container with sharp internal corners and then underfilling it with a liquid. In essence, the system is a large-scale version of micro heat pipe with regions of low capillary pressure. For an isothermal completely wetting system, the liquid will coat all of the walls of the chamber. On the other hand, for a finite contact angle system, some of the walls will have only an extremely small amount (probably

Received 24 May 2002; revision received 9 December 2002; accepted for publication 29 December 2002. Copyright © 2003 by the authors. Published by the American Institute of Aeronautics and Astronautics, Inc., with permission. Copies of this paper may be made for personal or internal use, on condition that the copier pay the $10.00 per-copy fee to the Copyright Clearance Center, Inc., 222 Rosewood Drive, Danvers, MA 01923; include the code 0887-8722/03 $10.00 in correspondence with the CCC.

*Graduate Student, Isermann Department of Chemical Engineering.
†Graduate Student, Isermann Department of Chemical Engineering; currently Research Scientist, Research Center, Engelhard Corporation, Iselin, NJ 08830.
‡Distinguished Research Professor, Isermann Department of Chemical Engineering; wayner@rpi.edu. Member AIAA.
§Professor, Isermann Department of Chemical Engineering; plawsky@rpi.edu.

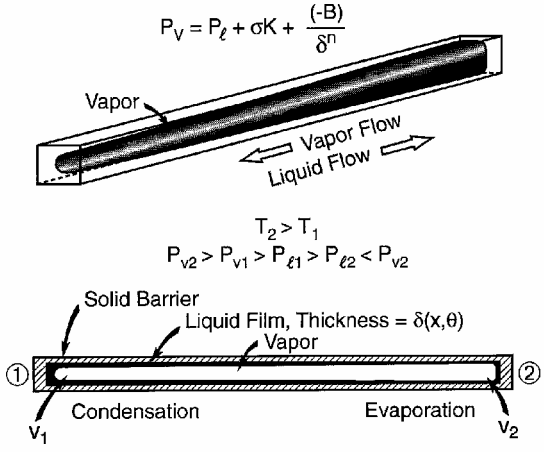

Fig. 1 Constrained vapor bubble; assumptions for schematic: $B < 0$ for wetting system with heat input at 2, heat removal at 1, and $g \rightarrow 0$.

less than a monolayer) of adsorbed vapor, which changes the surface properties of the solid–vapor interface. Liquid will fill at least a portion of the corners in both cases. If temperature $T_2 > T_1$ because of an external heat source in the evaporator and heat sink in the condenser, energy flows from 2 to 1 by conduction in the walls and by an evaporation, vapor flow, and condensation mechanism (Fig. 1). The condensate flows from 1 to 2 due to the intermolecular force field, which is a function of the film thickness profile. The film thickness profile is a function of the thermal conditions on the surface. There is a shape-dependent pressure jump at the vapor–liquid interface, $P_v - P_l$, due to the anisotropic stress tensor near interfaces. The pressure jump is given by the extended Young–Laplace equation, which includes the effects of both capillarity, σK, and disjoining pressure Π:

$$P_v - P_l = \sigma K + \Pi \tag{1}$$

Because of the relatively large cross-sectional area for vapor flow in our system, the vapor space is almost isobaric.

The classical Young–Laplace equation of capillarity has been successfully used to describe the pressure jump at a curved liquid–vapor interface under equilibrium conditions, see for example, Concus.[1] Examples of its use to describe nonequilibrium fluid dynamics in micro heat pipes and grooves are given by Peterson and Ha,[2] Wu and Peterson,[3] and Khrustalev and Faghri.[4] In these cases, the pressure jump causing fluid flow is a function of the liquid–vapor surface tension and the interfacial radius of curvature. This leads to the extended Young–Laplace model for the pressure jump at the liquid–vapor interface (see Refs. 5–17). These long-range van der Waals forces have been found to be extremely important in that they lead to the concept of an extended evaporating meniscus and the Kelvin–Clapeyron model for interfacial heat transfer, for example, see Refs. 6, 10, 16, and 18–20. Long-range intermolecular forces in the thin film control the liquid bridges connecting corners of the CVB.

We find that relatively large systems (millimeter compared to micrometer) and small pressure gradients in the thicker thin-film regions are needed for both optimum heat flux performance and convenient experimental study. However, as presented in Fig. 1, these large systems are easily distorted by the Earth's gravitational field. Because of the sensitivity of systems of this size to gravity and to small temperature and pressure gradients, these thermal systems need to be finally studied under the microgravitational conditions of intended use. "Axisymmetric" systems with small Bond numbers are required for optimum performance. (The term axisymmetric is used herein to mean reflective symmetry with respect to the length axis.) The Bond number gives the effect of gravity on the configuration of the interface with components in both the axial direction and cross-sectional plane. The cross-sectional Bond number can be used to classify the various studies. In our case, the inside width and height are 3 mm, giving a $Bo = 2.8$ for ethanol at 25°C, which indicates that the system will be asymmetric for horizontal or inclined cells. For the horizontal cell, the curvature changes by approximately 1000 between the top and bottom of the cell. Therefore, a vertical cell is used for ground studies.

Throughout the CVB system under microgravity conditions, fluid flows as a result of the intermolecular forces of liquid–liquid cohesion and liquid–solid adhesion. This pressure field for flow results from an imposed external temperature field that causes a nonuniform liquid film to form due to evaporation/condensation. When a quartz cell is used, the pressure field is revealed by optically measuring and analyzing the shape of the liquid volume by viewing the naturally occurring interference pattern through a microscope. The pressure field and resulting transport processes can be studied at the molecular, microscopic, and macroscopic levels. At the junction of the liquid film with the vapor and the solid substrate (which can have a nonevaporating adsorbed film), the liquid film thickness can be (but does not need to be) the thickness of a monolayer. This junction has been called the contact line or interline and is of general importance to the field of wetting. The contact line thickness is controlled by the imposed experimental conditions. A monolayer thickness can be obtained by imposing a large superheat at the contact line. At the other end of the nonisothermal CVB, where condensation occurs, the thickness of the liquid film can be much larger (approximately 1.5 mm). Therefore, depending on the experimental conditions, extremely large variations in the thickness scale are possible. Under some nonisothermal conditions, the heat flux in the contact line region can be enormous. On the other hand, the flux can be substantially less a short distance away, where the film thickness is much larger, and so this device exhibits an enormous range in both the scale and the level of transport processes. For example, under equilibrium conditions, it is a thermodynamic cell in which interfacial properties can be accurately studied.[17] Under nonequilibrium conditions, a very dynamic transport system can be studied. The ultimate goal is to determine how this system can be optimized for use as a passive heat exchanger under microgravity conditions.

The following broad categories can be evaluated in the CVB under microgravity and normal gravity conditions: 1) effect of intermolecular forces, temperature, and liquid–vapor volume ratio on the isothermal equilibrium liquid film thickness profile, for example, DasGupta et al.[17]; 2) effect of intermolecular forces, liquid–vapor volume ratio, and temperature on the average phase change transport processes over a relatively large area, that is, the overall macroscopic heat flow rate, average fluid flow rate, heat conductance, and stability results presented subsequently; and 3) effect of intermolecular forces, liquid–vapor volume ratio, and temperature on phase change over a very small area, that is, the local heat flux distribution, local fluid flow rate, and stability. These areas of research can be further subdivided with the adjectives transient and steady state, and, in the Earth's environment, vertical and approximately horizontal. Although gravity does not affect the horizontal pressure gradient in our current Earth-bound studies, the horizontal cell does give different results in the top and bottom sections, which affect each other in a complicated way. On the other hand, the pressure gradient due to gravity in a vertical cell adversely affects the maximum flux and range of measurements. There are advantages and disadvantages associated with both orientations in a strong gravitational field. Herein, experimental and theoretical results on the vertical CVB are presented. Another engineering objective is to use these results to design heat transport systems uniquely suited to microgravity conditions

The CVB studies are generic with uses beyond those associated with heat pipes. Nevertheless, it is useful to relate the current system to a micro heat pipe[21] about which Peterson[22] and Faghri[23] have written excellent reviews. Many papers have been published on the modeling of micro heat pipes. Cotter's[21] original work described a model to predict the behavior of micro heat pipes. However, this model requires the knowledge of a parameter that behaves as a correction factor. Babin et al.[24] present a steady-state model that assumes prior knowledge of the liquid film profile to compute the liquid and vapor pressure drops. Longtin et al.[25] developed a one-dimensional

model to predict the operating parameters of the micro heat pipe. The factor they use to compare their model results to experiments is the macroscopic heat flux instead of a more fundamental parameter such as the film curvature profile. Bowman et al.[26,27] derived an expression for a constant area, adiabatic end condition, heat pipe efficiency and compared the performance of a heat pipe fin with a standard fin. Khrustalev and Faghri[4] and Swanson and Peterson[28] used models based on the extended Young–Laplace equation to analyze a micro heat pipe. Heat transfer from a stable evaporating thin film in the neighborhood of a contact line was analyzed by Moosman and Homsy[12] and Brown et al.[29] Swanson and Herdt[30] used the three-dimensional extended Young–Laplace equation to describe the details of the evaporating meniscus in a capillary tube. Catton and Stroes[31] presented a one-dimensional, semi-analytical model for prediction of the wetted length supported by inclined triangular capillary grooves subject to heating below. Karthikeyan et al.[32] studied the intermediate region of the horizontal CVB using a one-dimensional model; however, they used an average heat transfer coefficient over the entire evaporator length. Although these studies provide a considerable insight into the evaporation mechanism in the grooved surfaces, they did not correlate interfacial curvature profiles of the meniscus directly with temperature profiles. In this paper, we present the results of our Earth-based experimental measurements of the temperature and interfacial curvature profiles of the vertical CVB. A simplified model, which provides insights into the heat transfer and fluid flow phenomena underlying the evaporator region, is derived for the first time to correlate the curvature profile directly with the experimental temperature data under microgravity and in the Earth's environment.

Experimental Studies

Figure 2 shows a schematic diagram of the vertical CVB experimental setup. The CVB was formed by underfilling an evacuated fused quartz cell with 99.99% pure ethanol. The quartz cell had a square cross-section with sharp internal corners and internal dimensions of $3 \times 3 \times 40$ mm. A thermoelectric heater was located on the top, and coolers on each side of the cell were located at 20 mm from the top. The fill ratio determines the bubble length, which is the bottom of the vapor bubble. If the bubble were too long, the coolers would block observations and measurements of a portion of the evaporator and the whole portion of the condenser region. If it were too short, coolers would have little effect on the operation.

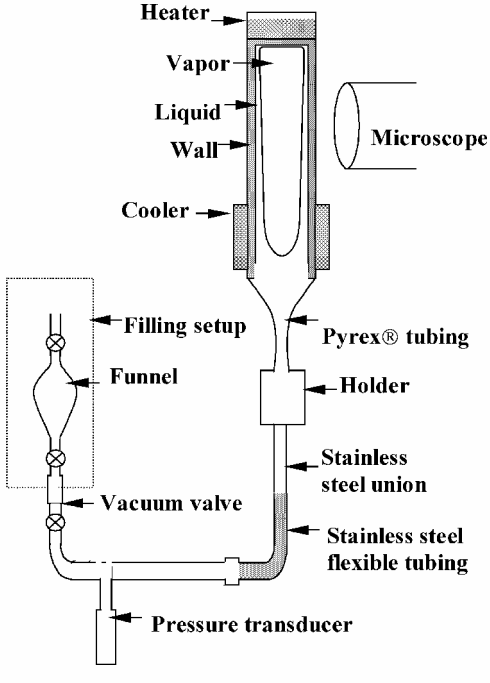

Fig. 2 Vertical constrained vapor bubble system; thermocouples on the outside flat wall of the cell not shown.

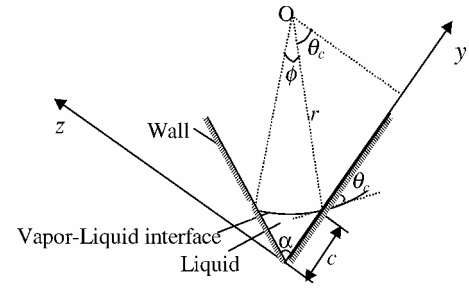

Fig. 3 One of the corners of a container with a vertex angle α.

We use the measured bubble length to characterize our system. In our CVB system, the bubble length is 16 mm. An in situ LabView® data acquisition system was built to measure the temperature profile. Details regarding the experimental setup may be seen by Wang et al.[33] There were 12 microscale K-type (chromel–alumel) thermocouple beads pasted onto a side of the cell; the distance between the thermocouples was 2 mm. The 12th thermocouple was used to measure room temperature. The uncertainty of the absolute temperature measurement was 0.5°C. Because we only dealt with the temperature difference, the overall uncertainty was further reduced. A pressure transducer was connected to the system through a three-way vacuum valve to monitor continuously the vapor–liquid system pressure. Pressure measurements indicate that we had less than 6% noncondensibles.

A high-power microscope was rotated and situated on an adjustable stage, so that the interference fringes in the side corner of the vertical CVB could be viewed and evaluated using image analyzing interferometry.[17,34] Monochromatic light ($\lambda = 543.5$ nm) from a Hg arc was used to illuminate the cell through a 50× objective of the microscope. With the 50× objective, each of the 640×480 pixels measures the average reflectivity (thickness) of a region with a diameter of 0.1777 μm. The interference fringes resulting from the reflection of monochromatic light at both the liquid–vapor and liquid–solid interfaces in the CVB were used to determine the thickness profile of the meniscus. Figure 3 shows one of the corners of the cell with a general vertex angle of α. In our particular case of square cross section, $\alpha = \pi/2$. The corner is partially filled with the liquid that forms an apparent finite contact angle of θ_c on the interior wall of the container. The coordinate axes are labeled in Fig. 3. The z axis represents the liquid film thickness δ. The y axis, which corresponds to one side of the container wall, represents the location of the film thickness profile. The plane of y–z is normal to CVB axis. The major portion of the vapor–liquid interface can and is assumed to be a part of a circle, the center of which is located at point $\mathcal{O}$. The coordinate of point $\mathcal{O}$ $(r\cos\theta_c,\ c + r\sin\theta_c)$ is easily derived from geometric relations, where $c = r[\sin(\phi/2)/\sin(\alpha/2)]$ and $\phi = \pi - (2\theta_c + \alpha)$. Thus, the shape of the vapor–liquid interface at the corner of a container can be expressed as

$$(\delta - r\cos\theta_c)^2 + (y - c - r\sin\theta_c)^2 = r^2 \tag{2}$$

When Eq. (2) is rearranged while using the negative square root,

$$y = c + r\sin\theta_c - \sqrt{r^2 - (\delta - r\cos\theta_c)^2} \tag{3}$$

The two unknowns, r and θ_c, can be obtained simultaneously by best fitting the experimental film thickness profile,

$$\min\left[\sum_{i=1}^{N}(y_{\mathrm{exp},i} - y_{\mathrm{cal},i})^2\right]$$

where N is the total number of dark and bright fringes. The subscripts exp and cal denote the experimental data and calculated values using Eq. (3), respectively. The curvature K is obtained from the reciprocal of the radius of curvature. The uncertainty in the value of curvature in the region between $x = 3$ and 6 mm is within 6% because the number of fringes available for data fitting is more than 6; however,

in the region between $x = 0$ and 3 mm, the uncertainty becomes large, up to 20%, because the number of fringes available for data fitting is reduced to 2 or 3. The detailed error analysis regarding the curvature measurements, which are a function of wavelength of the light, refractive index, apparent contact angle, interfacial curvature, and number of dark fringes, used for the data fitting is given by Zheng et al.[35]

Theoretical Analysis

In the evaporator region of the CVB, as shown in Fig. 4, the temperature gradient causes evaporation of the liquid, and the liquid recedes into the corner of the cell, which results in a curvature gradient driving the condensate up against gravity and shear stresses. The curvature distribution is the result of a pressure balance based on capillarity, gravity, and shear stress. Thus, the temperature gradient leads to the curvature gradient. Experimentally, the curvature and temperature profiles along the axial direction of the cell can be measured. Herein, we explore a theoretical relationship between the curvature and temperature profiles.

Neglecting the effect of a possible superheated liquid, we made the following assumptions to derive governing equations for the model:

1) There is steady-state operation.

2) There are constant fluid properties. Because the vapor space is relatively large and the pressure drop in the vapor phase is very small, it is reasonable to assume an approximately constant vapor temperature. Thus, we can evaluate the fluid properties at this vapor temperature.

3) The flow is laminar and incompressible. It is expected that the Reynolds numbers of the liquid and vapor are less than 10, and the Mach number for the vapor is much smaller than unity at the operating temperature of the CVB. Therefore, both liquid and vapor flows are assumed to be incompressible.

4) There is a single radius of curvature. Because the interfacial radius of curvature parallel to the CVB axis is much larger than that normal to the CVB axis, the mean radius of curvature at any axial location is equal to the radius of curvature normal to the CVB axis. This was justified by Karthikeyan et al.[32] and Huang et al.[36]

5) The radius of curvature is constant at any axial location. The thicker portion of the meniscus has a constant radius of curvature at any axial position. This radius of curvature will be used to analyze axial flow. Additional models are needed to analyze transverse flow and the contact line.

6) The effect of Marangoni flow can be neglected.

7) The liquid film profile in the corner is static.

An energy balance on the quartz wall gives a second-order differential equation

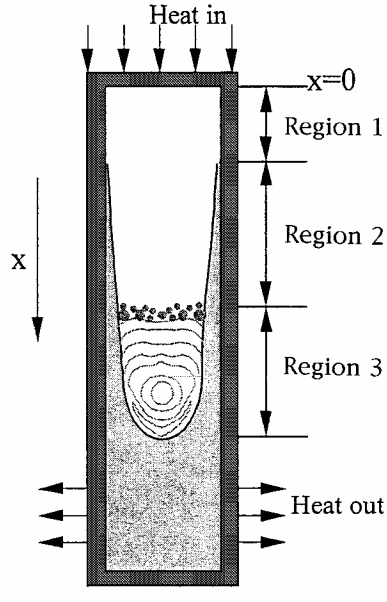

Fig. 4 Schematic of three different regions of the vertical CVB.

$$kA\frac{d^2T}{dx^2} - h_o(T - T_\infty)p - mh_{fg} = 0 \tag{4}$$

Note that the third term represents the heat flow rate per unit axial length and m represents the rate of evaporation per unit axial length from the evaporator wall into the vapor phase.

We define the total rate of evaporation from the beginning of the evaporator to an axial location x as

$$\Gamma(x) \equiv \int_0^x m\,dx \tag{5}$$

Rearranging Eq. (4) and substituting into Eq. (5) yields

$$\Gamma(x) = \frac{kA}{h_{fg}}\frac{dT}{dx}\bigg|_0^x - \frac{h_o p}{h_{fg}}\int_0^x (T - T_\infty)\,dx \tag{6}$$

To use Eq. (6), the experimental outside surface temperature profile of the evaporator was fitted as a polynomial and then substituted into Eq. (6).

The conservation of mass for liquid in the evaporator gives

$$\frac{d(\rho_l A_l U_l)}{dx} + m = 0 \tag{7}$$

The average liquid velocity can be obtained from the total rate of evaporation, which, in turn, can be determined from the experimental temperature profile.

The governing equation for the liquid momentum balance is expressed as

$$A_l\frac{dP_l}{dx} + A_l\rho_l g\sin\beta + \frac{d\left(\rho_l U_l^2 A_l\right)}{dx} - L_{lw}\tau_{lw} = 0 \tag{8}$$

The first term represents the pressure difference that pumps the liquid against gravity and shear stresses. It is related to the curvature gradient using the Young–Laplace equation:

$$\frac{dP_l}{dx} = -\sigma_l\frac{dK}{dx} \tag{9}$$

For Eq. (9), it is assumed that the axial component of the disjoining pressure gradient is small. The second term in Eq. (8) is the gravitational term. For our vertical CVB with the heater at the top, $\beta = -(\pi/2)$. The third term in Eq. (8) accounts for the change in the bulk momentum flow. Because the liquid velocity is small, this term can be neglected compared to the other terms. The fourth term is the tangential force that arises due to the shear encountered at the liquid–wall interface. This shear stress is due to friction and is written as

$$\tau_{lw} = \tfrac{1}{2}\rho_l U_l^2 f \tag{10}$$

where the friction factor is $f = k_f/Re$ and k_f is a constant that depends on the geometry of the flow channel. The Reynolds number is defined as $Re = -(d_h U_l \rho_l/\mu_l)$ (note negative sign of U_l), where the hydraulic diameter is $d_h = 4A_l/8r$, the liquid cross-sectional area is $A_l = 2C_l r^2$, and C_l is the geometric coefficient of the liquid cross-sectional area.

Combining Eqs. (8–10) yields a differential equation describing the curvature profile in the CVB:

$$\frac{dK}{dx} = -\frac{k_f\mu}{C_l^3\rho_l\sigma_l}\Gamma(x)K^4 - \frac{\rho_l g}{\sigma_l} \tag{11}$$

where $\Gamma(x)$, a function of axial location, can be obtained from the experimental temperature profile using Eq. (6). The curvature profile can then be solved numerically from the experimental temperature profile.

The boundary condition for Eq. (11) is

$$K|_{x=0} = K_0 \tag{12}$$

where K_0 is an assumed large curvature at the beginning of the evaporator ($x = 0$). K_0 is adjusted to fit the experimental curvature at the end of the evaporator (which is relatively small and, thus, accurate to measure).

For an isothermal case, $\Gamma = 0$, and Eq. (11) becomes

$$\Delta K = -(\rho_l g/\sigma_l)\Delta x \tag{13}$$

which equates the capillary pressure with the hydrostatic pressure.

Under microgravity, the gravitation term is neglected in Eq. (11), and the equation is solved by separation and integration.

$$\frac{1}{K^3} - \frac{1}{K_0^3} = \frac{3k_f\mu}{C_l^3\rho_l\sigma_l}\int_0^x \Gamma(x)\,\mathrm{d}x \tag{14}$$

If the temperature of the evaporator is also close to the temperature of the surroundings (at low heat input), or we prevent heat loss to the surroundings, the heat loss term in Eq. (6) can be neglected. For this reason, the following simpler equation, which provides insight into the heat transfer and fluid flow phenomena underlying the evaporator region in microgravity, is derived and correlates the curvature profile directly with the experimental temperature data:

$$\frac{1}{K^3} - \frac{1}{K_0^3} = \frac{3k_f\mu kA}{C_l^3\rho_l\sigma_l}[T(x) - T(0)] \tag{15}$$

Results and Discussions

For a vertical CVB under isothermal conditions, there is a thin liquid film in the corner along the entire axial direction. In the thicker portion of the meniscus, the capillary pressure equals the hydrostatic pressure, which can be expressed by Eq. (13). When the heaters and coolers are turned on, the thin film in the corner evaporates and recedes into the corner of the CVB. Compared to the isothermal CVB, the curvature gradient of a nonisothermal CVB is larger, thereby increasing the available pumping force to pump the liquid up to the evaporator against gravitational and viscous forces. As the heat input increases, a dryout region appears, where no thin film exists in the corner, and the radius of curvature of the film is zero. If the heat input is increased further, the dryout region grows longer and moves toward the cooler end. Therefore, there are two or three regions in the CVB depending on the heat input.

Figure 5 shows the temperature profile of the CVB filled with ethanol at a heat input from the power meter of 0.49 ± 0.08 W. There are dryout, evaporation, and condensation regions. For comparison, the temperature profile of the dry cell with the same temperature at the beginning of the cell is also shown in Fig. 5. The temperature profile of the dry cell can be described by the standard fin equation, obtained by neglecting the third term on the left side of Eq. (4). The outside heat transfer coefficient h_o, which includes natural convection and radiation heat transfer, was obtained by best fitting temperature profile of the dry cell using the fin equation. Figure 6 shows temperature profiles of the dry cell and fin equation fitted curves at different heat inputs. Table 1 lists the value of h_o at different heat inputs. The average value of 20.95 ± 1.5 W/m^{2}K

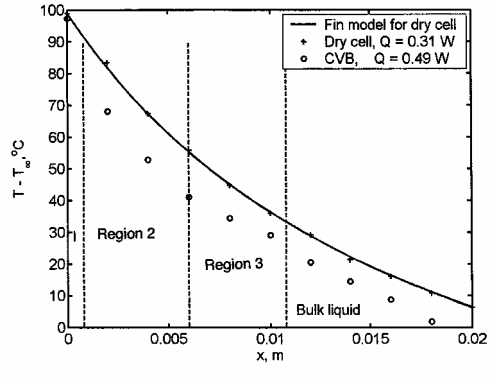

Fig. 5 Comparison of temperature profiles of the dry cell with the CVB using ethanol; $T - T_\infty \pm 0.5$°C.

Table 1 Outside heat transfer coefficient h_o obtained at different heat inputs

Quantity	1	2	3	4	5	Average
Q, W	0.93	0.81	0.66	0.55	0.28	——
h_o, W/m^2 K	20.95	21.50	21.50	21.15	19.65	20.95

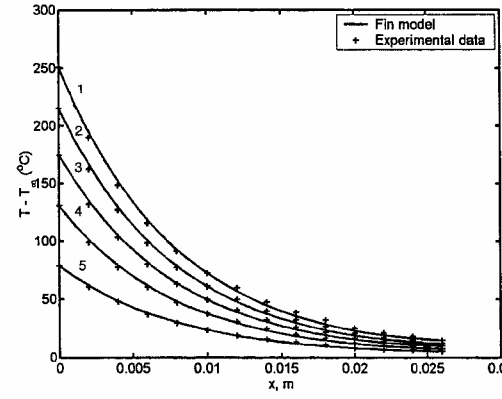

Fig. 6 Surface temperature profiles for the dry cell.

is chosen as the outside heat transfer coefficient. As can be seen from Fig. 5, the temperature profiles of the CVB deviated from those of the dry cell due to evaporation and condensation processes. The heat transport rates were higher than those of the dry cell. We measured the vapor pressure using a pressure transducer and found that it correlated with the expected vapor pressure based on the surface temperature in the region of condensation. Because of the large cross-sectional area of the vapor space, the pressure in the vapor space has to be approximately constant. For the isothermal system, at room temperature, $T_\infty = 23.8$°C, we measured the correct saturated vapor pressure of $P_v = 8193.4$ Pa, which did not change over a period of many months. Therefore, we did not have a leak and, within the measurements, maintained a good vacuum. The outside surface temperature of the dry quartz cell responded to heat flux as expected. We have also operated various vertical cells that responded the same way. On the other hand, the horizontal cells (see Karthikeyan et al.[32]) behaved differently as to the axial temperature profiles. For this horizontal cell, the temperature profile was uniform over a significant portion of the cell as expected for a heat pipe. Possible reasons for the measured temperature gradient in wet vertical cell are 1) poor conduction in the quartz because the temperatures were measured on the flat portion of wall away from the meniscus region and 2) possibility of a superheated liquid. We need the low thermal conductivity quartz to see the fluid profile. Additional three-dimensional analyses beyond this presentation are needed to model the complicated temperature field that indicates a superheated liquid in a wall region next to a dry region. However, the measurements of the vapor pressure for different conditions over a period of months indicated that there was a low level of noncondensibles present.

Figures 7 and 8 show interference patterns of the liquid film at different locations of the evaporator region. The bright part indicates the presence of a nonevaporating thin film on the flat surface. At a location closer to the top of the evaporator as shown in Fig. 7, the spacing between fringes is smaller, indicating a larger curvature, $K = 7100$ m^{-1}. In Fig. 8, $K = 5300$ m^{-1}. The resulting pressure gradient in the fluid drives the liquid from the region of condensation toward the region of evaporation. Figure 9 shows the film in the corner of the cell at the junction that separates region 2 from region 3. At the top of Fig. 9, $K = 3600$ m^{-1}. On the flat surface of the cell, the vapor condensed into discrete liquid drops, which were then absorbed into the bulk liquid in the corner. The interference fringes representing the liquid film in the corner were spread out due to the condensation of the vapor. Closer to the cooler, the condensate formed a continuous, thicker liquid film on the flat surface of the glass. As heat input rates increased, the droplet condensation region disappeared and was replaced completely by film condensation.

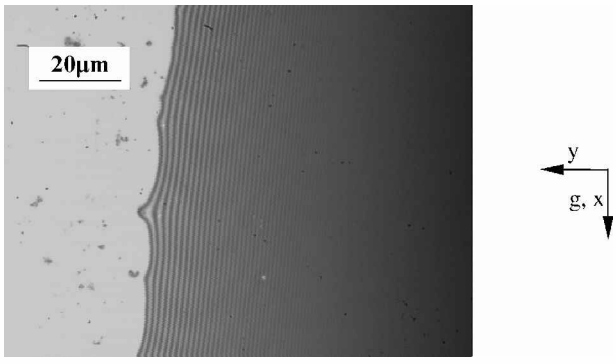

Fig. 7 Interference fringes of the thin film of ethanol in the corner of the cell at $x = 2.8 \pm 0.1$ mm, $K = 7100\ \mathrm{m}^{-1}$.

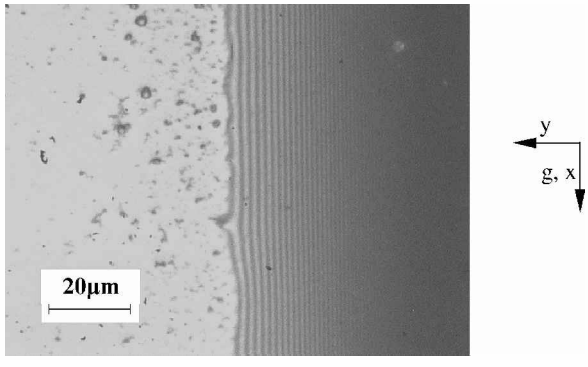

Fig. 8 Interference fringes of the thin film of ethanol in the corner of the cell at $x = 4.8 \pm 0.1$ mm, $K = 5300\ \mathrm{m}^{-1}$.

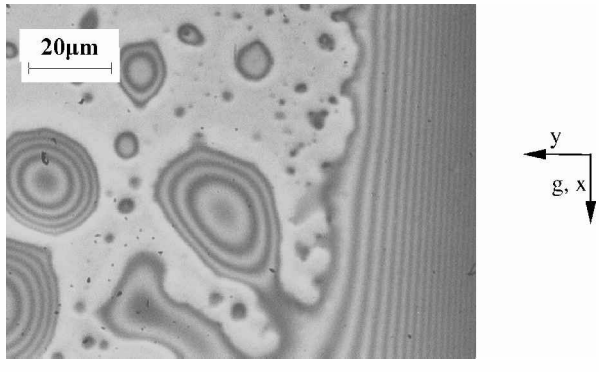

Fig. 9 Interference fringes of the thin film of ethanol in a region around the junction, $x = 6.0 \pm 0.1$ mm, which separates region 2 from region 3; $K = 3600\ \mathrm{m}^{-1}$.

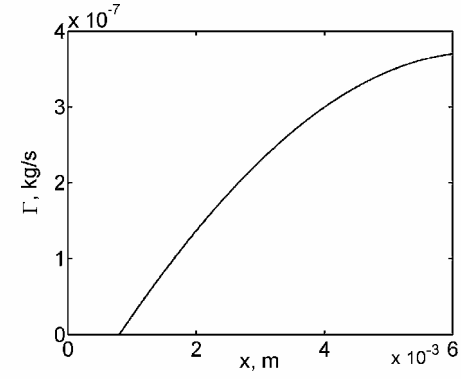

Fig. 10 Total rate of evaporation in the evaporator between $x = 0$ and x.

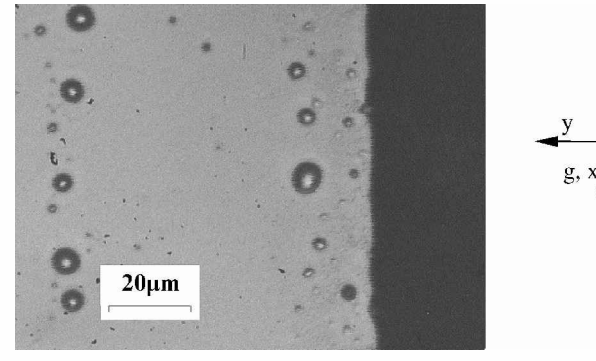

Fig. 11 Dry region.

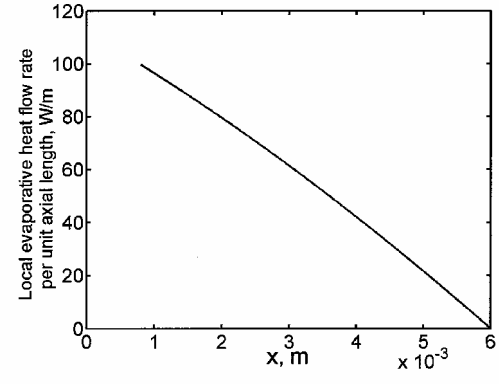

Fig. 12 Local evaporative heat flow rate per unit axial length in the evaporator.

Figure 10 shows the profile of the total rate of evaporation from the beginning of the evaporator to an axial location x obtained from Eq. (4). Based on the definition of $\Gamma(x)$, the rate of evaporation m per unit length at any axial location corresponds to the slope of $\Gamma(x)$: $m = \mathrm{d}\Gamma/\mathrm{d}x$. The slope at the beginning of the evaporator is the largest and indicates the largest rate of evaporation. This is justified because the film is thinnest and the temperature difference between the wall and vapor phase is the largest at this location. The slope of $\Gamma(x)$ decreases as x increases along axial location, indicating that the rate of evaporation decreases. At $x = 6$ mm, the slope $\Gamma(x)$ approaches zero, which indicates the end of the evaporation and the evaporator region of the CVB (junction of regions 2 and 3). Note that the location of the end of the dryout region where $r \to 0$ is determined as follows: First, we estimate it from the comparison of temperature profiles of the dry cell and the CVB with ethanol (Fig. 5). The length of the dry region is determined by obtaining overlapping regions of temperature profiles of the dry cell and the CVB.[37] In our case, extrapolating the temperature profile of the evaporator region of the CVB, we found that the dryout region ends at about $x = 0.8$ mm. Then, interferometry is used to obtain accurately the length of dry region as follows. Interference fringes of the thin film can be clearly observed at the top of the vertical cell when no heat is input to the cell. As heat input increases, the liquid recedes into the corner, and the number of interference fringes observed become fewer. When heat input is large enough, no fringes are observed, and the dry region appears, as shown in Fig. 11. The dry region moves downward as heat input increases further. The location of the end of the dry region was read accurately from the three-way translation stage. Using this approach, we found that the end of the dry region occurred at $x = 0.8$ mm. Figure 12 shows the local evaporative heat flow rate per unit axial length in the evaporator. The heat flow rate is the largest at 0.8 mm and then decreases as it goes toward the cooler end. The heat flow rate reaches zero at 6 mm, which indicates the end of evaporation. The film thickness profiles corresponding to interference patterns in Figs. 6–8 are shown in Fig. 13. The plus sign represents the experimental data, and the solid line represents the calculated results from Eq. (3). As can be seen, the film thickness profile becomes steeper

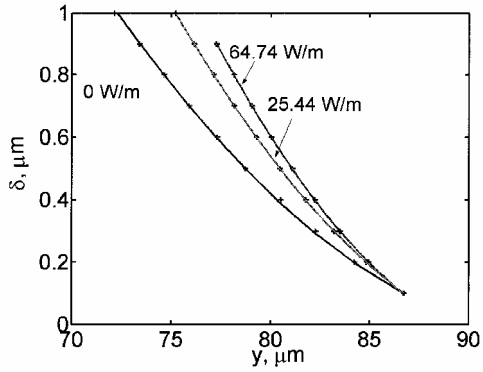

Fig. 13 Film thickness profiles at different local evaporative heat flow rates corresponding to Fig. 12. Absolute value of the error in film thickness is a function of film thickness but always within 5%.

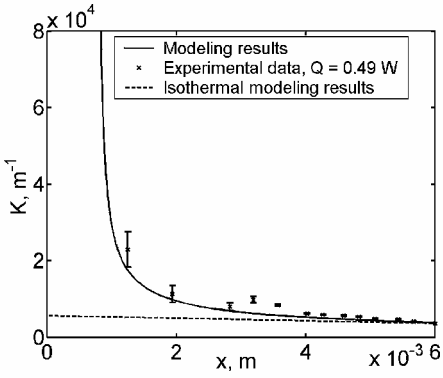

Fig. 14 Comparison of the experimental curvature data with modeling results.

as the heat flow rate increases, which indicates the larger interfacial curvature.

Solving Eq. (11) numerically by employing the results of $\Gamma(x)$ from the temperature profile gives the curvature profile, as shown in Fig. 14. The experimentally measured curvature data were obtained using the image analyzing technique described earlier. The experimental data were in good agreement with the modeling results from Eq. (11). Currently, it is difficult to obtain nonisothermal experimental curvature values in excess of 25,000 m^{-1}. However, we are working on image processing enhancement techniques that would extend this range considerably. For comparison, the modeling result of the isothermal CVB represented by a dashed line [calculated by Eq. (13)] is also shown in Fig. 14. This model was previously confirmed experimentally by Wang et al.[34] The curvature gradient of the isothermal CVB is very small. We find, for the nonisothermal CVB, the evaporation/condensation process causes the curvature to deviate from that of the isothermal CVB. The curvature increases gradually from $x = 6$ mm. In the region close to the top, the curvature increases dramatically, indicating more evaporation, which is consistent with the profile of $\Gamma(x)$. As the heat input was increased, the top of the cell started to dry out, and the curvature gradient became larger. This provided a larger driving force for liquid to flow upward to the evaporator against both gravity and shear stresses.

Conclusions

1) Experimental techniques for measuring temperature and interfacial curvature profiles were developed and used to study heat transfer and fluid flow in the evaporator section of a vertical CVB.

2) Experimental results for a large Bond number were obtained for future comparison with experimental results to be obtained in microgravity (low Bond number with the same system).

3) A mathematical model was developed to predict the curvature profile of the thin film in the evaporator. The measured curvature profiles were in good agreement with modeling results. The concept of the total rate of evaporation as a function of axial position $\Gamma(x)$ was introduced. The slope of $\Gamma(x)$ at the beginning of the evaporator is the largest, which indicates the largest rate of evaporation, then decreases as x increases in the axial direction, which indicates that the rate of evaporation decreases.

4) A theoretical relation that correlates interfacial curvature directly with temperature profiles in the Earth's environment was developed.

5) An analytical expression [Eq. (15)], which reveals an inherent relation between temperature and interfacial curvature profiles under microgravity conditions, was derived for future use.

Acknowledgments

This material is based on work supported by NASA under Grant NAG3-1834, NAG3-2383.

References

[1]Concus, P., "Static Menisci in a Vertical Right Circular Cylinder," *Journal of Fluid Mechanics*, Vol. 34, Pt. 3, Dec. 1998, pp. 481–495.

[2]Peterson, G. P., and Ha, J. M., "Capillary Performance of Evaporating Flow in Microgrooves: An Approximate Analytical Approach and Experimental Investigation," *Journal of Heat Transfer*, Vol. 120, No. 3, 1998, pp. 743–751.

[3]Wu, D., and Peterson, G. P., "Investigation of the Transient Characteristics of a Micro Heat Pipe," *Journal of Thermophysics and Heat Transfer*, Vol. 5, No. 2, 1991, pp. 129–134.

[4]Khrustalev, D., and Faghri, A., "Thermal Analysis of a Micro Heat Pipe," *Proceedings of National Heat Transfer Conference*, HTD Vol. 236, American Society of Mechanical Engineers, New York, 1993, pp. 19–30.

[5]Derjaguin, B. V., Nerpin, S. V., and Churaev, N. V., "Effect of Film Transfer upon Evaporation of Liquids from Capillaries," *Bulletin Réunion Internationale des Laboratoires D'essais et de Recherches sur les Matériaux et les Constructions*, No. 29, 1965, pp. 93–98.

[6]Potash, M., Jr., and Wayner, P. C., Jr., "Evaporation from a Two-Dimensional Extended Meniscus," *International Journal of Heat and Mass Transfer*, Vol. 15, Oct. 1972, pp. 1851–1863.

[7]Blake, T. D., "Investigation of Equilibrium Wetting Films of n-alkanes on a-alumina," *Journal of the Chemical Society, Faraday Transactions*, Pt. 1, Vol. 71, No. 2, 1975, pp. 192–208.

[8]Teletzke, G. F., Scriven, L. E., and Davis, H. T., "How Liquids Spread on Solids," *Chemical Engineering Communications*, Vol. 55, May–June 1987, pp. 41–82.

[9]Renk, F., Wayner, P. C., Jr., and Homsy, G. M., "On the Transition between a Wetting Film and a Capillary Meniscus," *Journal of Colloid and Interface Science*, Vol. 67, No. 3, 1978, pp. 408–414.

[10]Kamotani, Y., "Evaporator Film Coefficients of Grooved Heat Pipes," *Proceedings of 3rd International Heat Pipe Conference*, AIAA, Reston, VA, 1978, pp. 128–130.

[11]Holm, F. W., and Goplen, S. P., "Heat Transfer in the Meniscus Thin-Film Transition Region," *Journal of Heat Transfer*, Vol. 101, Aug. 1979, pp. 543–547.

[12]Moosman, S., and Homsy, S. M., "Evaporating Menisci of Wetting Fluids," *Journal of Colloid and Interface Science*, Vol. 73, Jan. 1980, pp. 212–223.

[13]Truong, J. G., and Wayner, P. C., Jr., "Effect of Capillary and Van der Waals Dispersion Forces on the Equilibrium Profile of a Wetting Liquid: Theory and Experiment," *Journal of Chemical Physics*, Vol. 87, Oct. 1987, pp. 4180–4188.

[14]Wayner, P. C., Jr., "The Effect of Interfacial Mass Transport on Flow in Thin Liquid Films," *Colloids and Surfaces*, Vol. 52, No. 1, 1991, pp. 71–84.

[15]Wong, H., Morris, S., and Radke, C. J., "Two-dimensional Menisci in Nonaxisymmetric Capillaries," *Journal Colloid and Interface Science*, Vol. 148, No. 1, 1992, pp. 284–287.

[16]DasGupta, S., Schonberg, J. A., and Wayner, P. C., Jr., "Investigation of an Evaporating Extended Meniscus Based on the Augmented Young–Laplace Equation," *Journal of Heat Transfer*, Vol. 115, 1993, pp. 201–208.

[17]DasGupta, S., Plawsky, J. L., and Wayner, P. C., Jr., "Interfacial Force Field Characterization in a Constrained Vapor Bubble Thermosyphon," *AIChE Journal*, Vol. 41, Sept. 1995, pp. 2140–2149.

[18]Wayner, P. C., Jr., Kao, Y. K., and LaCroix, L. V., "The Interline Heat Transfer Coefficient of an Evaporating Wetting Film," *International Journal of Heat and Mass Transfer*, Vol. 19, May 1976, pp. 487–492.

[19]Wayner, P. C., Jr., "Effect of Thin Film Heat Transfer on Meniscus Profile and Capillary Pressure," *AIAA Journal*, Vol. 17, July 1979, pp. 772–776.

[20]Stephan, P. C., and Busse, C. A., "Analysis of the Heat Transfer Coefficient of Grooved Heat Pipe Evaporator Walls," *International Journal of Heat and Mass Transfer*, Vol. 35, Feb. 1992, pp. 383–391.

[21] Cotter, T. P., "Principles and Prospects of Micro Heat Pipes," *Proceedings of the 5th International Heat Pipe Conferences*, The Japanese Association for Heat Pipes, Tokyo, Japan, 1984, pp. 328–335.

[22] Peterson, G. P., "Overview of Micro Heat Pipe Research and Developments," *Applied Mechanics Review*, Vol. 45, No. 5, 1992, pp. 175–189.

[23] Faghri, A., "Heat Pipe Science and Technology," 1st ed., Taylor and Francis, Washington, DC, 1995, pp. 624–671.

[24] Babin, B. R., Peterson, G. P., and Wu, D., "Steady State Modeling and Testing of a Micro Heat Pipe," *Journal of Heat Transfer*, Vol. 112, Aug. 1990, pp. 595–601.

[25] Longtin, J. P., Badran, B., and Gerner, F. M., "A One-Dimensional Model of a Micro Heat Pipe During Steady State Operation," *Journal of Heat Transfer*, Vol. 116, Aug. 1994, pp. 709–715.

[26] Bowman, W. J., Moss, T. W., Maynes, D., and Paulson, K. A., "Efficiency of a Constant-Area, Adiabatic Tip, Heat Pipe Fin," *Journal of Thermophysics and Heat Transfer*, Vol. 14, No. 1, 1999, pp. 112–115.

[27] Bowman, W. J., Storey, J. K., and Svensson, K. I., "Analytical Comparison of a Constant Area, Adiabatic Tip, Standard Fins, Heat Pipe Fins," *Journal of Thermophysics and Heat Transfer*, Vol. 13, No. 2, 1999, pp. 269–272.

[28] Swanson, L. W., and Peterson, G. P., "The Interfacial Thermodynamics of Micro Heat Pipes," *Journal of Heat Transfer*, Vol. 117, Feb. 1993, pp. 195–201.

[29] Brown, J. R., Chang, W. S., Halliman, K. P., and Chebaro, H. C., "Heat Transfer from Stable Evaporating Thin Films in the Neighborhood of a Contact Line," *Proceedings of National Heat Transfer Conference*, American Society of Mechanical Engineers, New York, 1993, pp. 1–8.

[30] Swanson, L. W., and Herdt, G. C., "Model of the Evaporating Meniscus in a Capillary Tube," *Journal of Heat Transfer*, Vol. 114, May 1992, pp. 434–441.

[31] Catton, I., and Stroes, G. R., "A Semi-Analytical Model to Predict the Capillary Limit of Heated Inclined Triangular Capillary Grooves," *Journal of Heat Transfer*, Vol. 124, No. 1, 2002, pp. 162–168.

[32] Karthikeyan, M., Huang, J., Plawsky, J., and Wayner, P. C., Jr., "Experimental Study and Modeling of the Intermediate Section of the Nonisothermal Constrained Vapor Bubble," *Journal of Heat Transfer*, Vol. 120, No. 2, 1998, pp. 166–173.

[33] Wang, Y.-X., Plawsky, J., and Wayner, P. C., Jr., "Heat and Mass Transfer in a Vertical Constrained Vapor Bubble Heat Exchanger Using Ethanol," 34th National Heat Transfer Conf., Paper NHTC2000-12201, American Society of Mechanical Engineers, New York, Aug. 2000.

[34] Wang, Y.-X., Zheng, L., Plawsky, J., and Wayner, P. C., Jr., "Optical Evaluation of the Effect of Curvature and Apparent Contact Angle in Droplet Condensate Removal," *Journal of Heat Transfer*, Vol. 124, No. 8, 2002, pp. 729–738.

[35] Zheng, L., Wang, Y.-X., Plawsky, J., and Wayner, P. C., Jr., "Accuracy of Measurements of Curvature and Apparent Contact Angle in a Constrained Vapor Bubble Heat Exchanger," *International Journal of Heat and Mass Transfer*, Vol. 45, May 2002, pp. 2021–2030.

[36] Huang, J., Karthikeyan, M., Plawsky, J., and Wayner, P. C., Jr., "Heat Transfer and Fluid Flow in a Nonisothermal Constrained Vapor Bubble," *Chemical Engineering Communications*, Vol. 181, Sept. 2000, pp. 203–223.

[37] Basu, S., "Experimental Study and Thermal Modeling of the Constrained Vapor Bubble Heat Pipe Operation in a Convection-Free Environment Under the Influence of Gravity," Ph.D. Dissertation, Chemical Engineering Dept., Rensselaer Polytechnic Inst., Troy, NY, Jan. 2002.